Lawrence Livermore National Laboratory

Observation of pedestal mode spreading into SOL and broadening of divertor particle flux width on EAST tokamak

X Xu

November 2025

Nuclear Fusion

Disclaimer

This work performed under the auspices of the U.S. Department of Energy by Lawrence Livermore National Laboratory under Contract DE-AC52-07NA27344.

nuclear fusion
IAEA

PAPER • OPEN ACCESS

Observation of pedestal mode spreading into SOL and broadening of divertor particle flux width on EAST tokamak

To cite this article: T. Zhang *et al* 2025 *Nucl. Fusion* **65** 056019

OPEN ACCESS
IOP Publishing | International Atomic Energy Agency
Nuclear Fusion
Nucl. Fusion **65** (2025) 056019 (14pp)
https://doi.org/10.1088/1741-4326/adc74c

Observation of pedestal mode spreading into SOL and broadening of divertor particle flux width on EAST tokamak

T. Zhang[1,*], F.F. Long[2], G.S. Li[1], X.Q. Xu[3], J.B. Liu[1], K.N. Geng[1], Y.F. Wang[1], B. Zhang[1], K.X. Ye[1], Z.Q. Zhou[2], F.B. Zhong[4,5], F. Wen[1], N. Yan[1], X. Gao[1,*] and the EAST team[a]

[1] Institute of Plasma Physics, Chinese Academy of Sciences, PO Box 1126, Hefei, Anhui 230031, China
[2] School of Nuclear Science and Technology, University of Science and Technology of China, Hefei 230026, China
[3] Lawrence Livermore National Laboratory, Livermore, CA 94550, United States of America
[4] Advanced Energy Research Center, Shenzhen University, Shenzhen 518060, China
[5] Key Laboratory of Optoelectronic Devices and Systems of Ministry of Education and Guangdong Province, College of Optoelectronic Engineering, Shenzhen University, Shenzhen 518060, China

E-mail: zhangt@ipp.ac.cn and xgao@ipp.ac.cn

Received 20 September 2023, revised 18 March 2025
Accepted for publication 31 March 2025
Published 10 April 2025

Abstract

Pedestal turbulence spreading into a crape-off layer (SOL) can be used to explain the experimentally observed strong pedestal-SOL coupling and is expected to be important for the broadening of divertor deposition profiles in future devices (Xu *et al* 2019 *Nucl. Fusion* **59** 126039). In the EAST tokamak, it is found that an electromagnetic (EM) mode in the pedestal region can spread into the SOL and broaden the divertor particle flux width. Multi-channel fluctuation reflectometry is used to measure the density fluctuations at the plasma edge. The EM mode rotates in the electron diamagnetic drift direction in the lab frame with a frequency range of [40–90] kHz, toroidal mode number $n = 12$–13 and poloidal wavenumber $k_\theta = 0.41$ cm^{-1}. The mode amplitude peaks around the maximum of the pedestal density gradient. As the mode amplitude increases, the reflectometry channel in the SOL can clearly capture the mode. This result suggests that the EM mode is excited in the pedestal gradient region and spreads into the SOL. It is further found that the particle flux deposition profile in the divertor is broadened as the EM mode appears.

Keywords: pedestal mode, turbulence spreading, scrape-off layer, divertor deposition profile

(Some figures may appear in colour only in the online journal)

[a] See Gong *et al* 2024 (https://doi.org/10.1088/1741-4326/ad4270) for the EAST Team.
[*] Authors to whom any correspondence should be addressed.

1. Introduction

To achieve high fusion power, the plasma of future fusion devices will mainly operate in the high confinement mode (H-mode) with a divertor configuration [1, 2]. Most of the power will cross the separatrix and flow inside a narrow channel on open field lines in the scrape-off layer (SOL) which directly connects to the divertor target plates. Since parallel transport is much larger than perpendicular transport, the SOL heat flux width (λ_q) is generally small [3]. Based on the multi-machine experimental scaling law [4] in low-gas-puff H-mode tokamak plasma, it is inferred that the baseline plasma of ITER ($I_p = 15$ MA, $Q = 10$) might have a λ_q of approximately 1 mm. Such a narrow heat flux width will result in a peak heat load in the divertor target plate far exceeding the current value that the material can withstand. Although power dissipation through radiation in the divertor region can largely reduce the peak heat load, the operating window for the ITER baseline plasma will be narrower for smaller λ_q [5]. The new result in the high-density H-mode plasma shows that near-SOL pressure fall-off length upstream is close to Eich scaling in the low turbulent state, but increases in the high turbulent state [6], implying turbulence transport is effective in broadening the heat flux width. For ASDEX Upgrade plasmas in different confinement regions (L, I, H), λ_q is strongly correlated with the pedestal pressure gradient length, implying the impact of the pedestal on SOL [7]. One possible reason could be that the pedestal turbulence spreads into the SOL and has an influence on SOL transport.

Recent numerical simulation studies [8–10] show that the heat flux width in ITER might be larger than 4 mm, much broader than the extrapolated value (∼1 mm) based on experimental scaling. The mechanism could be that the neoclassical drift transport will decrease due to stronger magnetic field and larger device size, and turbulent transport will dominate [9, 10]. The key point in these simulations is that turbulence is excited in the pedestal gradient region and then spreads nonlinearly to the SOL region, thereby enhancing the perpendicular transport there. Turbulence spreading phenomena have been broadly observed in simulations/models and experiments for magnetically confined plasmas [11–20]. For H-mode plasma, the confinement improvement is due to turbulence suppression at the edge and a pedestal structure with steep gradient forms. Even with large E_r shear in this pedestal region, new turbulence modes can still be excited as observed in present devices [21–27], some of which make a significant contribution to pedestal transport. If these turbulence modes can spread into the SOL region, it is expected that the SOL perpendicular transport can be enhanced and the divertor particle or heat flux width can be broadened, as suggested by the simulations. There have been sporadic reports on the impact of pedestal turbulence modes on divertor deposition in recent years. In the quasi-continuous exhaust regime of the ASDEX Upgrade, λ_q is largely increased and the peak heat load is reduced, which can be attributed to the enhanced SOL perpendicular transport by the intermittent filament structure propagating from the pedestal region [28]. In HL-2A H-mode plasma, a pedestal coherent mode has the effect of redistributing the divertor particle flux [29]. In EAST (*Experimental Advanced Superconducting Tokamak)*, it is also observed that a coherent mode in the H-mode pedestal can increase the divertor particle flux width [30]. In the present paper, we will report the new result from the EAST tokamak. An electromagnetic (EM) mode is excited in the pedestal gradient region of the ELMy H-mode plasma heated by RF waves and can be observed in the far SOL region. The divertor particle flux width increases with the mode amplitude. The rest of this paper is organized as follows. The experimental setup is described in section 2. Section 3 presents the experimental results. The results are discussed in section 4, followed by a summary in section 5.

2. Experimental setup

EAST is a medium-sized tokamak with a major radius $R_0 = 1.85$ m and a minor radius $a = 0.45$ m. Two typical discharges (#87996 and #85131) have been selected for analysis. Both discharges are with an upper single null (USN) configuration and heated by RF waves. Figure 1 shows the plasma parameters for #87996 ($B_t = 2.2$ T, $I_p = 550$ kA, $q_{95} = 5$, $<n_e>/n_G = 0.6$–65) which is heated by lower hybrid wave (LHW) and electron cyclotron resonance heating (ECRH). The plasma enters H-mode at about 2.6 s and the shaded region indicates the phase for study, which is a relatively long ELM-free phase just before H–L back-transition. Here, the H–L back-transition could be due to the radiation power increase from impurity accumulation (figure 1(*d*)), resulting in net heating power close to the H-mode power threshold. It is observed that an EM mode in the pedestal can lead to a broadening of divertor particle flux width during the phase before H–L back-transition. This phenomenon is also observed during a relatively long time no-ELM phase in a sustained H-mode discharge #85131, which will be introduced and analyzed in the next section. Figure 2 shows the main diagnostics for the present data analysis. The density fluctuations are measured by multi-channel fluctuation reflectometry diagnostic close to midplane at the low field side (LFS). This diagnostic is composed of two sub-systems, i.e. O-mode polarized reflectometry [31] and X-mode polarized reflectometry [32]. For O-mode reflectometry, the cutoff frequency equals to the plasma frequency f_{pe},

$$f_{O,cutoff} = f_{pe} = \frac{1}{2\pi}\sqrt{\frac{n_e e^2}{\varepsilon_0 m_e}}.$$

For X-mode reflectometry at LFS, the cutoff frequency is,

$$f_{X,cutoff} = \frac{1}{4\pi}\left(f_{ce} + \sqrt{f_{ce}^2 + 4f_{pe}^2}\right).$$

where $f_{ce} = eB_0/(2\pi m_e)$ is the electron cyclotron frequency, e is the electron charge, ε_0 is the vacuum conductivity and m_e is the electron mass. Therefore, the O-mode reflectometry cutoff position only depends on electron density while that of the X-mode reflectometry depends on both the magnetic

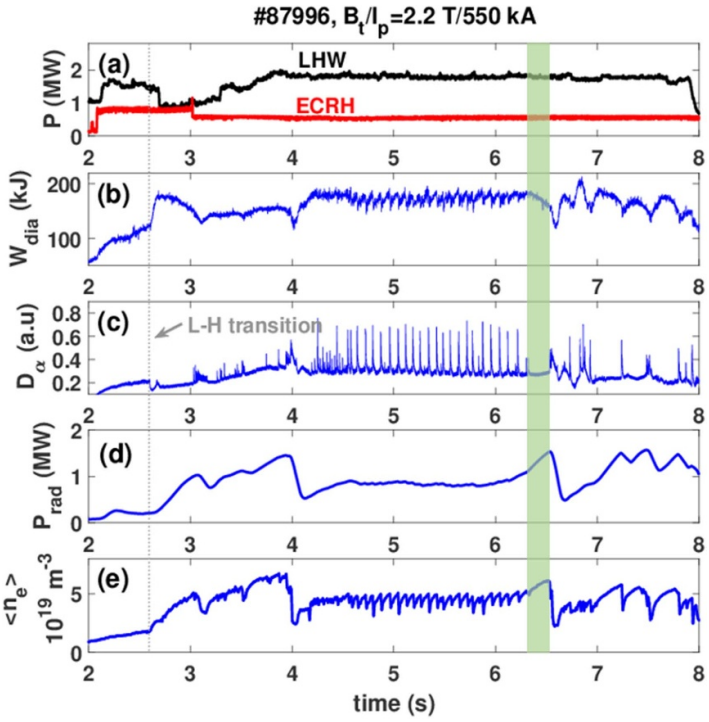

Figure 1. Parameters for EAST discharge #87996. (*a*) Heating power of LHW and ECRH, (*b*) diamagnetic energy $W_{\rm dia}$, (*c*) D_α signal, (*d*) radiation power and (*e*) line averaged density. The vertical dotted line indicates the first L–H transition time and the shaded region is for data analysis.

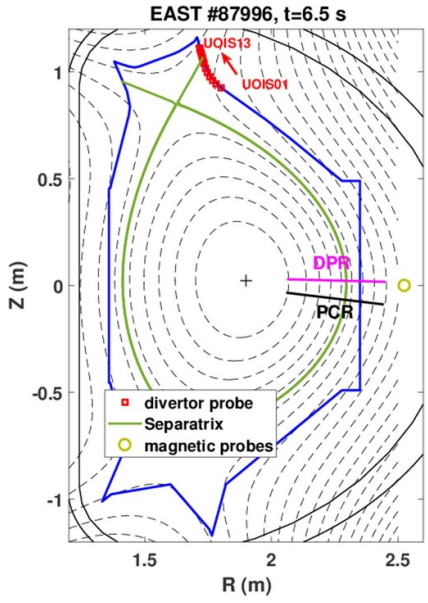

Figure 2. Plasma equilibrium for #87996 at $t = 6.5$ s and diagnostics for analysis, including density profile reflectometry (DPR), poloidal correlation reflectometry (PCR), magnetic probes mounted on vacuum vessel and divertor probes at upper outer divertor plate.

field and electron density. The diagnostics use two poloidally separated antennae for the receiver and therefore each frequency has two poloidal measurements, which can be used for poloidal correlation analysis. This diagnostic is thus usually called poloidal correlation reflectometry (PCR), whose view line is as shown in figure 2. High frequency magnetic probes with a sampling frequency of 1 MHz mounted on a vacuum vessel of L and K ports at LFS are used to measure the magnetic fluctuations. The toroidal distance between the magnetic probes of L and K is 22.5°, from which the toroidal mode number (n) of fluctuations with $n = 0$–16 can be determined. The electron density profile from the edge to the core is measured by density profile reflectometry (DPR), which is located at the LFS midplane with a horizontal view line. The time definition of the density profile can be up to 50 μs. Divertor triple Langmuir probe arrays (div-LPs) are installed at the lower and upper divertors including inner and outer tiles, respectively, and used for the measurement of ion saturation current ($j_{\rm s}$), from which the particle flux to divertor can be estimated as Γ_i (m^{-2}s^{-1}) $= n_{\rm t}Cs = js/e$ [33]. The plasmas presented in this paper are with USN configuration and so only upper outer divertor probes will be used, as shown in figure 2. There are 13 probes on the divertor plate, which are numbered UOIS01, UOIS02, …, UOIS13, where the probe UOIS13 is closest to the divertor corner.

3. Experimental result

In this section, a detailed analysis of the EM mode will be presented, mainly based on the discharge #87996 shown in figure 1 while the result for another discharge #85131 will also be shown. Figure 3 shows the fluctuation spectra for O-mode reflectometry at the lowest four frequencies (20.4 GHz,

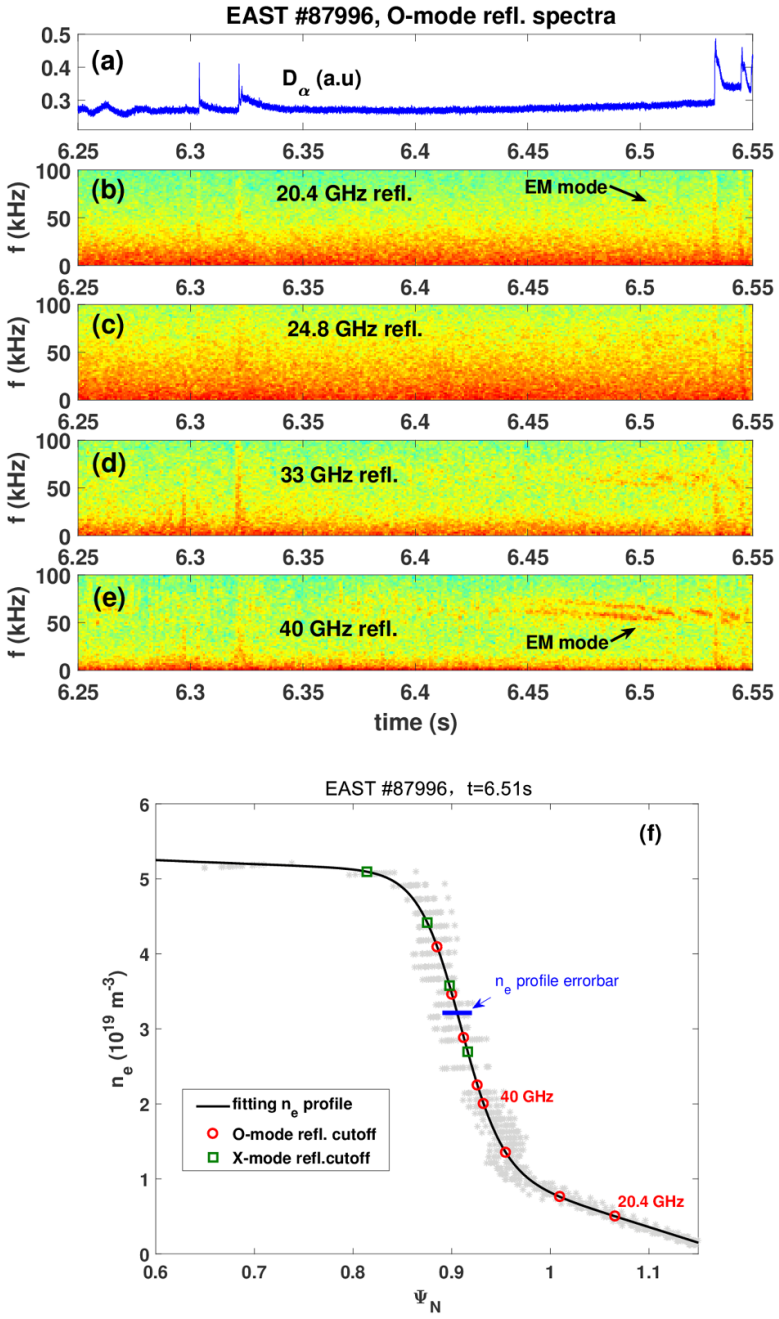

Figure 3. (*a*) D_α signal, (*b*)–(*e*) fluctuation spectra of O-mode reflectometry with frequency 20.4 GHz, 24.8 GHz, 33 GHz and 40 GHz respectively, (f) density profile at $t = 6.51$ s and the cutoffs for the multi-channel fluctuation reflectometry. The grey asterisk indicates the 20 density profiles obtained from 1 ms DPR data at around 6.51 s. The horizontal bar indicates a typical errorbar of the n_e profile.

24.8 GHz, 33 GHz and 40 GHz) in #87996. The cutoffs of the four reflectometry covering the pedestal gradient region to the far SOL ($\Psi_N = 0.93$–1.07) are shown in figure 3(*f*), where Ψ_N is the normalized flux coordinate and $\Psi_N = 1$ represents the separatrix. Here, the density profile is measured by DPR. Since the density profile has a time definition of 50 μs, a 1 ms data around at $t = 6.51$ s is analyzed and 20 density profiles can be obtained, as indicated by the grey asterisk in figure 3(*f*). The 20 density profile data are taken together and fitted, from which a smoothed density profile (black solid line in figure 3(*f*)) and then the cutoffs of PCR can be obtained. The errorbar of the density profile and PCR cutoffs can be calculated from the fitting error. The reflectometry is, essentially, a diagnostic to measure the radial position of the microwave cutoff layer. Therefore, the error in the density profile measured by reflectometry is mainly from the radial position as shown by the horizontal error bar in figure 3(*f*). It is observed from the 40 GHz reflectometry spectra in figure 3(*e*) that a 40–90 kHz mode appears in the later ELM-free phase. This mode can also be observed in the magnetic probes mounted on the

vacuum vessel, suggesting an EM mode. It will be shown in section 4 that the EM mode has a toroidal mode number of $n = 12$–13 and poloidal wavenumber $k_\theta = 0.41$ cm^{-1}, rotating in the electron diamagnetic drift (EDD) direction in the lab frame. As the EM mode amplitude increases, the reflectometry channel in SOL (20.4 GHz, $\Psi_N = 1.07$) also captures the mode as shown in figure 3(*b*). In order to further verify this point, a coherence analysis between the fluctuations from 40 GHz reflectometry (pedestal) and 20.4 GHz reflectometry (SOL) is conducted. The spectral squared coherence (γ^2) between any two signals (X and Y) is calculated by

$$\gamma^2 = \frac{|P_{XY}(f)|^2}{|P_{XX}(f)||P_{YY}(f)|}$$

$$\text{with } P_{XY}(f) = \frac{1}{N_{\text{ens}}}\sum_{i=1}^{N_{\text{ens}}} X_i(f)Y_i^*(f),$$

$$P_{XX}(f) = \frac{1}{N_{\text{ens}}}\sum_{i=1}^{N_{\text{ens}}} X_i(f)X_i^*(f).$$

where N_{ens} is the number of ensembles, $X_i(f)$ and $Y_i(f)$ are the Fourier transforms of the time series $X(t)$ and $Y(t)$ and subscript i is the ensemble index. $P_{XY}(f)$ is usually called cross power spectral density and $P_{XX}(f)$ or $P_{YY}(f)$ is auto-power spectral density. Figures 4(*a*) and (*b*) show the coherence analysis at different phases, i.e. the first half phase ($t = [6.35$–$6.45]$s) and the second half phase ($t = [6.48$–$6.53]$s), respectively. For the first half phase, the coherence level is all below the noise level. But for the second half phase, there is significant coherence beyond the noise level between the fluctuations of pedestal and SOL at EM mode frequency. This result shows that the 20.4 GHz reflectometry in the SOL region observes the EM mode at the second half phase.

Now we will show that the EM mode should be a fluctuation originating from the pedestal gradient region. Multi-channel fluctuation reflectometry can in principle give the radial profiles of density fluctuation levels for EM modes. However, it is usually not easy to estimate the density fluctuation level from reflectometry measurement [34]. What we are here interested in is the shape for the radial distribution of the EM mode and another manner similar to [35] will be adopted to present it. Since both density fluctuations measured by reflectometry and magnetic fluctuations measured by magnetic probes can observe the EM mode, the signal from one magnetic probe is chosen as a reference. The coherence analyses between fluctuations from reflectometry and the reference signal is conducted and the coherence values around the EM mode are calculated. The radial distribution of this coherence value is presented in figure 5, where the profile of the absolute density gradient is also shown. Here, the errorbar of the cutoff for each PCR channel is calculated based on the fitting error of the density profile in figure 3(*f*). It is seen that the coherence value is largest around the region with peak density gradient and generally decreases as the density gradient is reduced in the more inner and outer regions. This result indicates that the EM mode is a fluctuation excited around the pedestal gradient region. For the channel at 20.4 GHz, its cutoff is actually in the SOL region even considering the errorbar and its coherence value is also significant while the density gradient is much smaller than that of the pedestal. This suggests that the EM mode originates from a pedestal gradient region that spreads into the SOL. It should be noted that the channel at near-SOL (24.8 GHz, $\Psi_N = 1.01$) has a very low coherence value and the reason could be due to the relatively low signal noise ratio of this channel or the strong background fluctuations close to the separatrix submerging the EM mode.

The influence of the EM mode on divertor deposition is also studied. Figure 6 shows the j_s profiles measured by these probes in two different phases, one belongs to the first half phase without the EM mode and the other belongs to the second half phase with the EM mode. The j_s profile demonstrates double peaks as usually observed in this device [36]. The difference between the two j_s profiles is that the main peak close to the strike point decreases while the secondary peak in the far SOL increases when the EM mode appears. This trend can be seen more clearly from the time evolutions for the j_s of the two peaks, as shown in figure 7. The EM mode amplitudes in the pedestal and SOL are, respectively, represented by the integrated power in the frequency range [40–90] kHz from the fluctuation spectra of 48 GHz reflectometry and 20.4 GHz reflectometry, shown in figures 7(*f*) and (*g*). Since the EM mode originates from the pedestal gradient region, it is suitable here to use the 48 GHz reflectometry because it is located at about $\Psi_N = 0.91$, close to the position of the peak density gradient (figure 5). The EM mode in the pedestal appears at about 6.42 s and gradually increases. At the same time, the j_s close to the strike point represented by UOIS09 gradually decreases while that in the far SOL represented by UOIS03 gradually increases. In order to describe the width of the double-peaked j_s profile, an integrated with ($\lambda_{\text{js,int}}$) is introduced,

$$\lambda_{\text{js,int}} = \frac{\int (j_s - j_{s,\text{BG}})\,\mathrm{d}s}{j_{s,\text{max}} - j_{s,\text{BG}}}\frac{1}{f_x}$$

where $j_{s,\text{BG}}$ is the background value, $j_{s,\text{max}}$ is the maximum value, s is the coordinate along the divertor plate and f_x is the magnetic flux expansion. In fact, the definition of $\lambda_{\text{js,int}}$ here follows from the integral power width as defined in [37]. In the present calculation, we take the value of UOIS13 as $j_{s,\text{BG}}$ since this probe always has the lowest j_s. The f_x in the studied phase is nearly constant at about 4.85. The time evolution of ($\lambda_{\text{js,int}}$) is shown in figure 7(*h*). It is seen from this plot that the integrated width shows a gradual increase with the pedestal EM mode amplitude in figure 7(*f*) after about 6.42 s. The dependence of $\lambda_{\text{js,int}}$ and peak ion saturation current ($j_{s,\text{peak}}$) on the EM mode amplitude in pedestal are shown in figure 8. Here, we take the value from UOIS09 as an approximation of $j_{s,\text{peak}}$. It is seen that the integrated width generally increases with the EM mode amplitude. At the same time, the peak ion saturation current decreases with the mode amplitude. The above result suggests that the EM mode has the effect of broadening the particle flux profile and reducing the peak particle flux to the divertor.

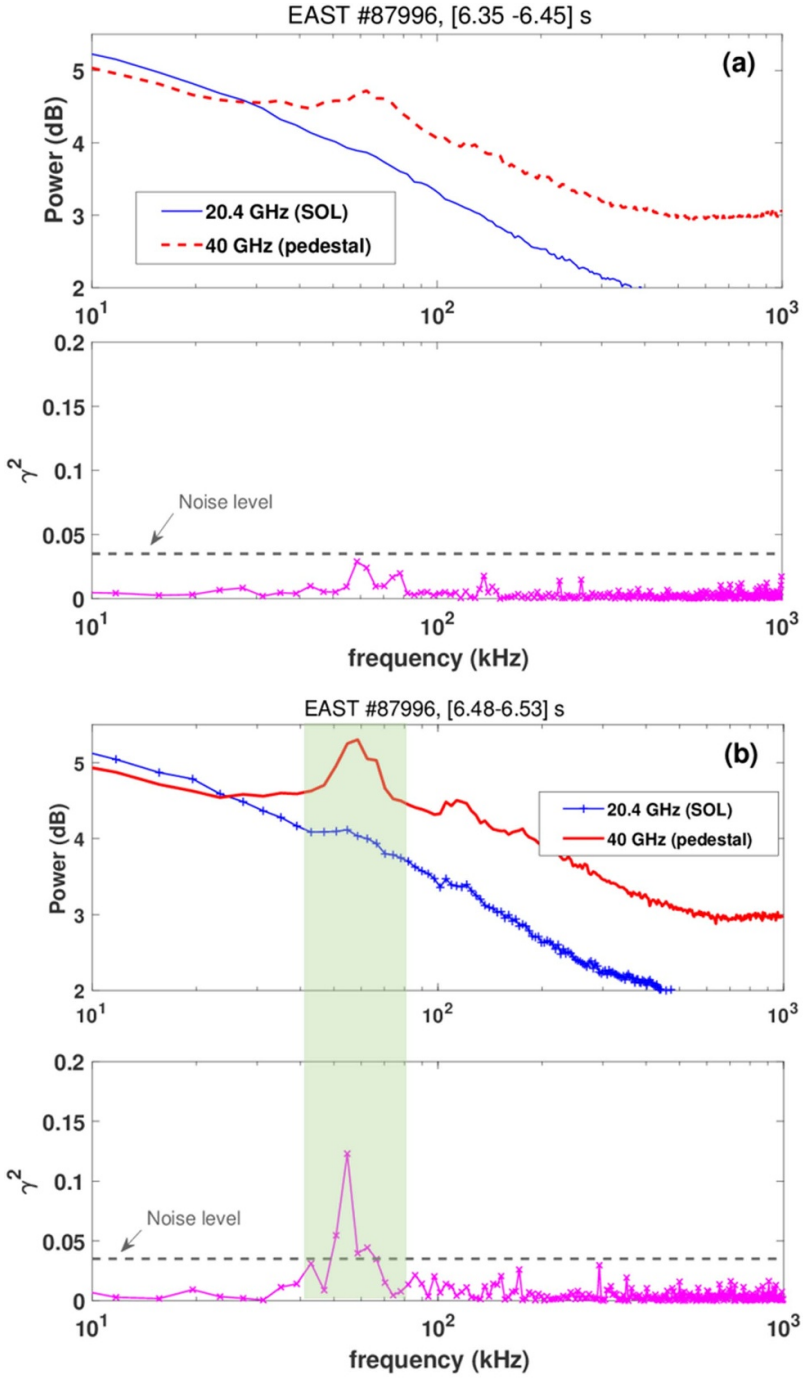

Figure 4. Auto-power spectra density for fluctuations measured by 40 GHz reflectomery and 20.4 GHz reflectomery and spectra squared coherence between the two signals at different phases. The shaded region indicates the EM mode.

In the above study for #87996, the electromagnetic mode appears in the long ELM-free phase just before the H–L back transition. In fact, the EM mode can also be observed in the inter-ELM phase in a normal H-mode plasma. However, the duration time of the EM mode is generally short (2–3 ms) in the inter-ELM phase and the broadening effect on the divertor particle flux width is not evident. In any case, there are some examples where the EM mode exists with a relatively long duration time in a normal H-mode plasma and the broadening effect on $\lambda_{\mathrm{js,int}}$ can be observed. Figure 9 shows one such discharge #85131, for which the plasma is $B_t = 2.28$ T, $I_\mathrm{p} = 500$ kA, $q_{95} = 5.2$ and heated by 1.8 MW LHW and 0.8 MW ECRH. The plasma shown in figure 9 enters the H-mode at ∼5.83 s and goes back to the L-mode at ∼7.56 s due to the switching-off of the LHW power. During this phase, the radiation power is less than 0.9 MW and the H-mode is sustained. Both regular ELMs and relatively long time no-ELM phase appear in this discharge. Figure 10 shows the

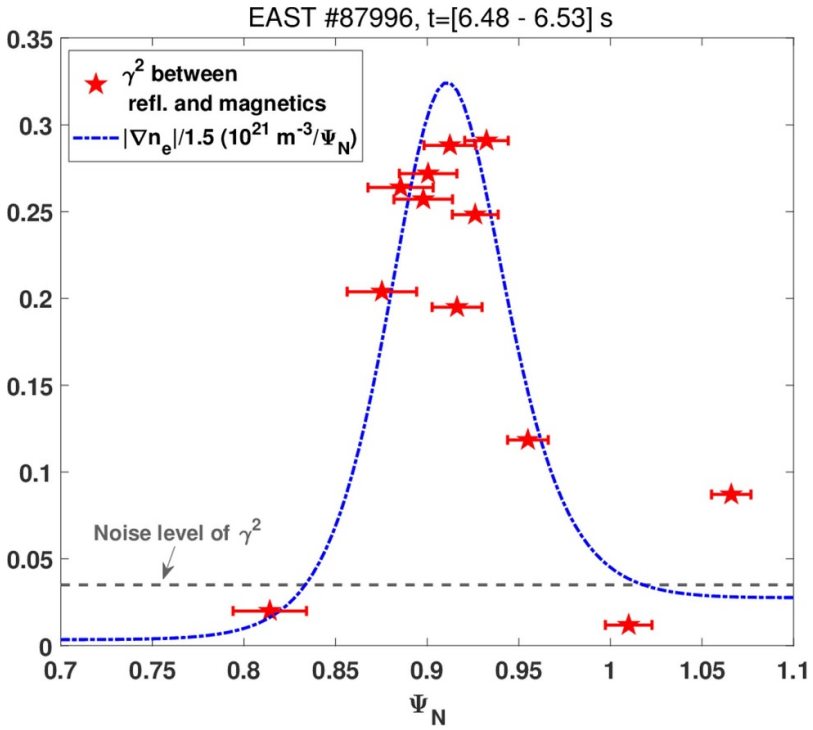

Figure 5. The star represents the spectra squared coherence between density fluctuation from reflectometry and magnetic fluctuation from magnetic probe for EM mode. The dashed line is the absolute value of density gradient divided by 1.5.

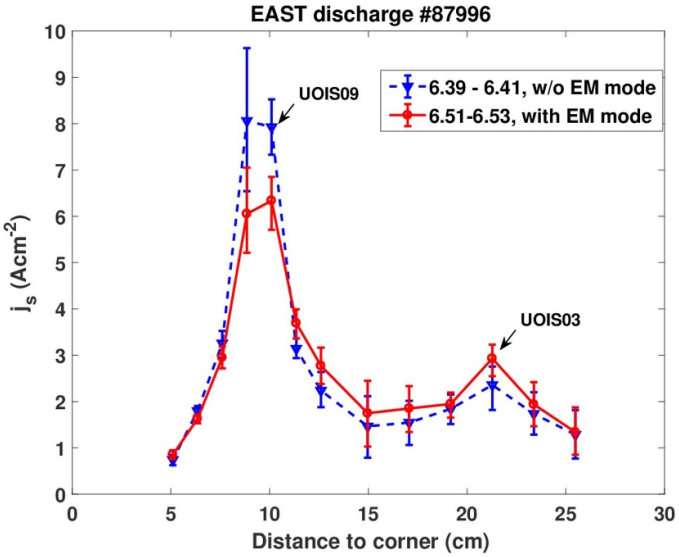

Figure 6. The j_s profiles at two different phases with and without EM modes.

observation of EM mode in the pedestal. The EM modes can be clearly observed in the long time no-ELM phase, as indicated by the shaded regions in figure 10(*b*) and persist for a relatively long time >15 ms. It is shown in figure 10(*c*) that the $\lambda_{\mathrm{js,int}}$ increases with the EM mode, demonstrating the broadening effect of the mode on the divertor particle flux width. It is noted that the EM mode is also observed in the later stage of the inter-ELM phase but the duration time is short (<3 ms). Although an increase in $\lambda_{\mathrm{js,int}}$ is also observed in the later stage of the inter-ELM phase, it is difficult to distinguish whether this increase is attributed to the EM mode or ELM.

4. Discussion of the results

We have shown that an EM mode with a frequency of [40–90] kHz is excited in the pedestal gradient region and can spread into the SOL, leading to broadening of the particle flux

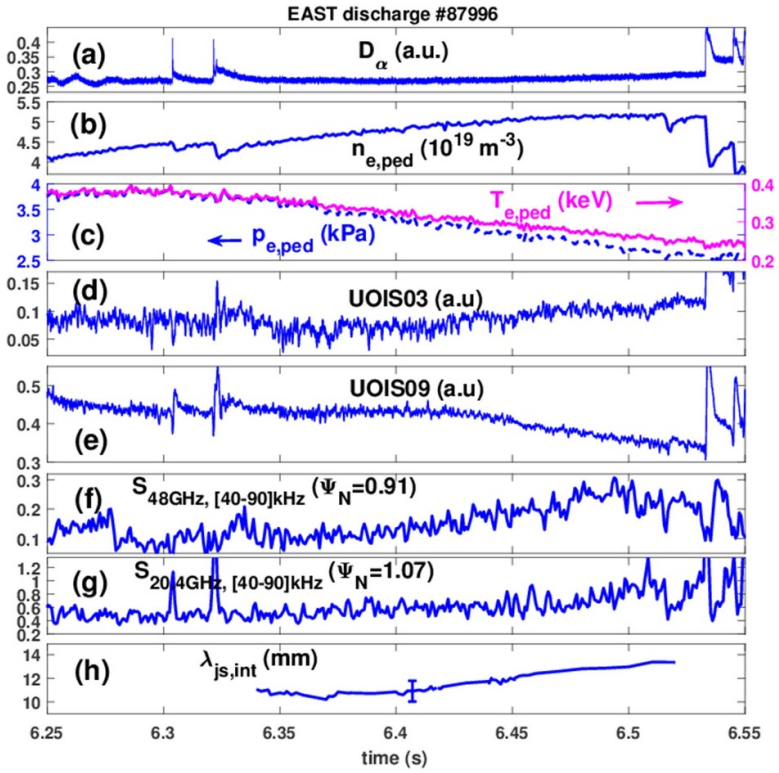

Figure 7. (*a*) D_α signal, (*b*) pedestal density ($n_{\mathrm{e,ped}}$), (*c*) pedestal electron temperature ($T_{\mathrm{e,ped}}$) and pressure ($p_{\mathrm{e,ped}}$), (*d*) signal of divertor probe UOIS03, (*e*) signal of divertor probe UOIS09, (*f*) fluctuation amplitude of EM mode at pedestal $\Psi_N = 0.91$, (*g*) fluctuation amplitude of EM mode at SOL, and (*h*) the integrated width ($\lambda_{\mathrm{js,int}}$) of divertor j_{s} profile.

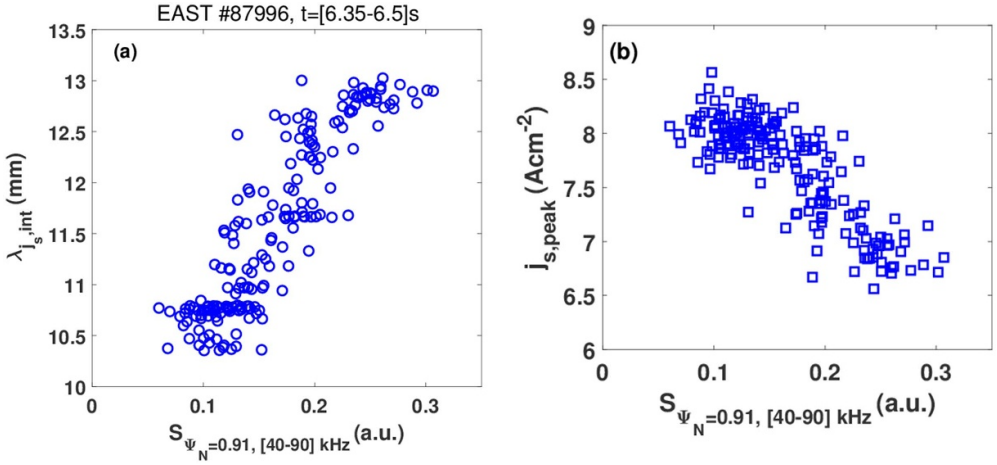

Figure 8. Dependence of $\lambda_{\mathrm{js,int}}$ and $j_{\mathrm{s,peak}}$ on EM mode amplitude in pedestal at $\Psi_N = 0.91$.

width deposited on the divertor plate. More characteristics will be presented in this section for further understanding.

The mode structure has been analyzed based on PCR and magnetic probes. The PCR uses two poloidally separated antennae to receive the reflected wave and poloidal correlation analyses can be made [31]. Figure 11(*a*) shows the local wavenumber-frequency spectra density, $S(k_\theta,f)$, calculated using the two-point correlation technique [38], for the 48 GHz reflectometry measurement at two different poloidal positions. Here, the poloidal separation at the cutoff surface is estimated to be about 0.9 cm. It is seen from the poloidal correlation analysis that the EM mode is propagating in the EDD direction. By integrating $S(k_\theta,f)$ in the EM mode frequency range [40–90] kHz, the local wavenumber spectral $S(k_\theta)$ for the EM mode is acquired, as shown in figure 11(*b*). The spectral weighted local wavenumber $\overline{k_\theta} = \int k_\theta S(k_\theta)\,\mathrm{d}k_\theta / \int S(k_\theta)\,\mathrm{d}k_\theta$ has been estimated to be about 0.41 cm^{-1}. The toroidal structure can be obtained by the coherence analysis of the magnetic fluctuations ($\delta \mathrm{b_L}$ and $\delta \mathrm{b_K}$) measured by magnetic probes in the L and K ports. Here, we will perform an indirect coherence

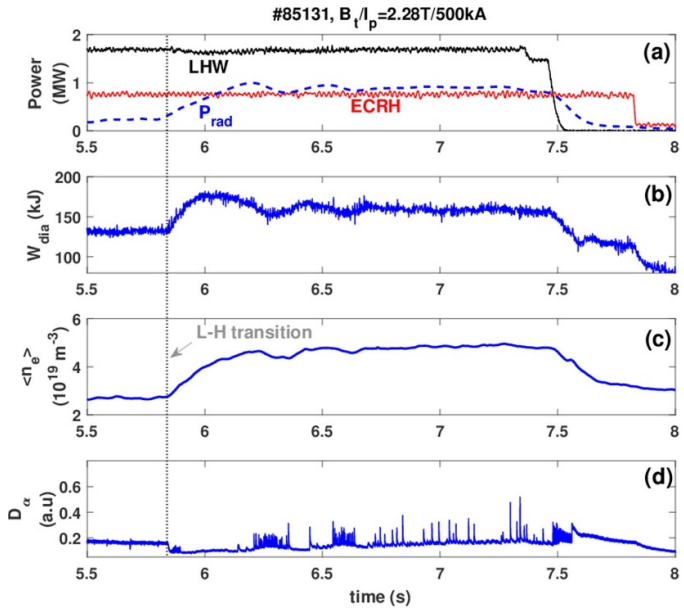

Figure 9. Parameters for EAST discharge #85131. (*a*) Heating power of LHW, ECRH and radiation power, (*b*) diamagnetic energy $W_{\rm dia}$, (*c*) line averaged density and (*d*) D_α signal. The vertical dotted line indicates the L–H transition time.

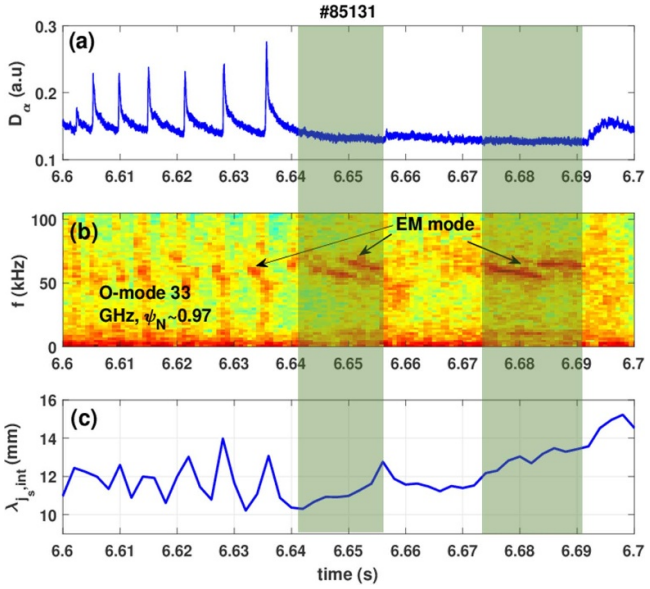

Figure 10. (*a*) D_α signal, (*b*) O-mode 33 GHz fluctuation reflectometry and (*c*) $\lambda_{\rm js,int}$. The shaded regions indicate the EM mode with a relatively long time duration.

analysis on $\delta b_{\rm L}$ and $\delta b_{\rm K}$ by taking reflectometry fluctuations as the intermediary. The coherence analysis is done between 48 GHz reflectometry fluctuation and $\delta b_{\rm L}/\delta b_{\rm K}$, respectively, as shown in figure 12(*a*). Significant coherence of the EM mode is observed for a frequency range from 50 to 65 kHz. Two cross-phases (ϕ_1 and ϕ_2) can be obtained from these coherence analyses and the difference of the two cross-phases, $\Delta\phi = \phi_1 - \phi_2$, is just the phase difference between $\delta b_{\rm L}$ and $\delta b_{\rm K}$. This indirect coherence analysis can largely suppress the background magnetic fluctuations shared by the magnetic probes and the information for the EM mode can be easily extracted. The dashed line in figure 12(*b*) shows $\Delta\phi$ from this calculation. The value of $\Delta\phi$ is positive, corresponding to a co-$I_{\rm p}$ rotation, which is in contradiction to the poloidal EDD direction as calculated from reflectometry fluctuations shown in figure 11. This could be due to the fact that the toroidal difference between the two magnetic probes exceeds half of the mode toroidal wavelength. A downshift of the 2π on $\Delta\phi$ has been applied and the corrected $\Delta\phi$ is represented as a solid line in figure 12(*b*). Figure 12(*c*) shows that the toroidal mode number is calculated from the corrected $\Delta\phi$. It is seen that an averaged toroidal mode number of the EM mode is about 12–13 and negative signs represents the mode rotating in the counter-$I_{\rm p}$ direction, consistent with the poloidal EDD direction. A further check on the consistency of the poloidal and toroidal structures is discussed as follows. If the EM mode is a flute-like mode, i.e. the wavenumber parallel to the magnetic field ($k_{//}$) is close to 0, there is a relation between the toroidal mode number and the local poloidal wavenumber [39]

$$n = R_{\rm mode} k_\theta \tan\alpha$$

where the $R_{\rm mode}$ is the major radius of the mode location and α is the pitch angle of the local magnetic field. For the EM mode, we use the parameters for the 48 GHz reflectometry to make the calculation, $k_\theta = 41\ {\rm m}^{-1}$, $R_{\rm mode} = 2.27$ m, $\alpha = 6.4°$. This results in a toroidal mode number n = 10–11, which is close to the value of n = 12–13 based on toroidal magnetic probe measurements. We have done the correlation analysis for #85131(t = [6.67 – 6.69]s) as shown in figure 13. The resulting toroidal mode number is also close to n = 12–13.

A comparison of the EM mode with other modes observed in EAST and in other devices is interesting. The most usually

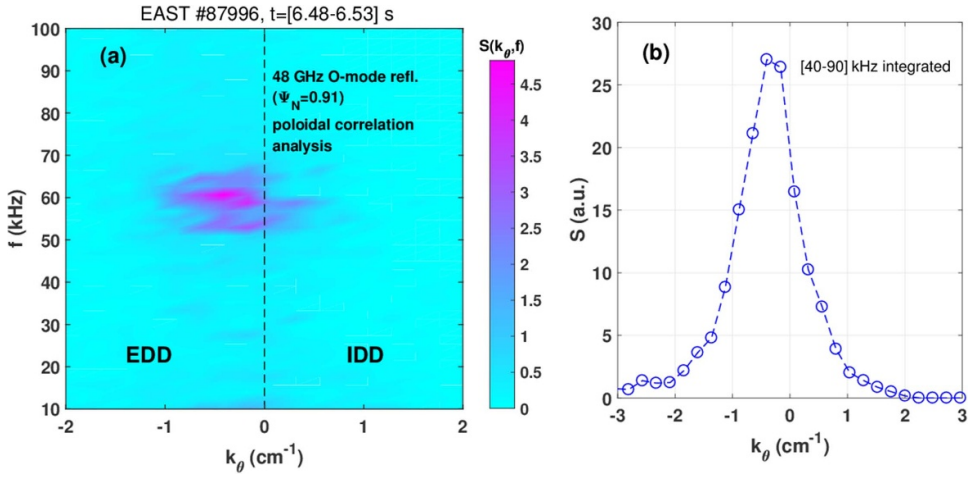

Figure 11. (*a*) Local spectral $S(k_\theta,f)$ calculated from 48 GHz reflectometry measurement at two different poloidal positions and (*b*) $S(k_\theta)$ by integrating local spectral from 40–90 kHz.

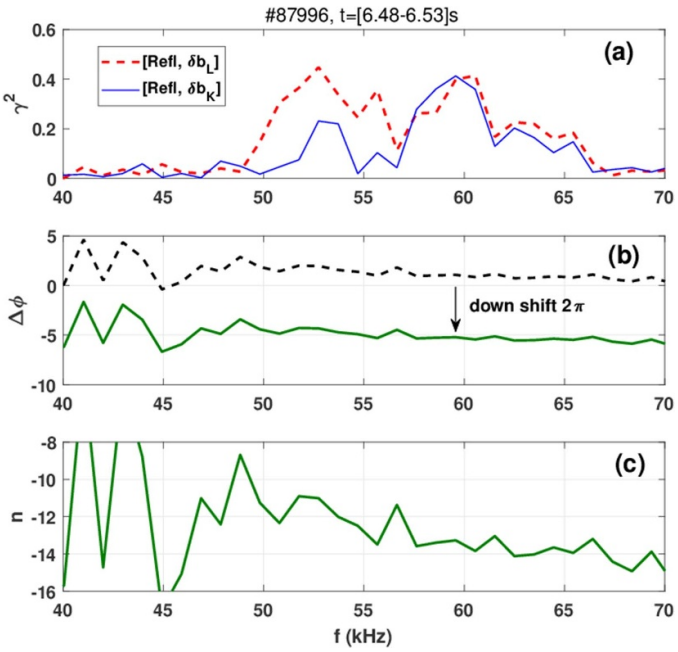

Figure 12. (*a*) The coherence between 48 GHz reflectometry fluctuation and magnetic fluctuations measured by L and K port magnetic probes, (*b*) the phase difference between L and K magnetic fluctuations and (*c*) the toroidal mode number.

observed modes in the H-mode pedestal on EAST is the edge coherent mode (ECM) [27, 40] and magnetic coherent mode (MCM) [41]. The ECM is a quasi-electrostatic mode with a toroidal mode number 12–17 and frequency range of [20–100] kHz and it can drive significant outward particle transport, leading to a broadening of the particle flux width on divertor [30]. The MCM is in the frequency range of 20–60 kHz and with a toroidal mode number $n = 1$, sometimes $n = 2$. MCM is mainly observed by magnetic probe and generally can not be observed in density and temperature fluctuations. Therefore, MCM is not expected to drive particle or heat transport. Both ECM and MCM rotate in the EDD direction in the lab frame, the same to the EM mode in present study. But ECM and MCM usually present with single frequency band while the EM mode usually presents with two or more frequency bands as shown in figure 3(*e*). On DIII-D, an EM mode with several bands, dubbed Modulating Pedestal Mode (MPM), appears in the long ELM-free phase before H-L back-transition [42]. The characteristics of MPM are as follows: frequency from 40 to 100 kHz with multiple frequency components, toroidal wave number (n) 3 or 4, poloidal wavenumber (k_θ) at outer mid-plane (OMP) of $\sim$0.3 cm^{-1}, propagating in the EDD direction in lab frame, located in the pedestal region and demonstrating ballooning structure, i.e. mainly in LFS. Table 1 presents a comparison between MPM of DIII-D and EM mode of EAST. The two modes present some similar and some different features. Both are pedestal EM modes, propagating in EDD direction in

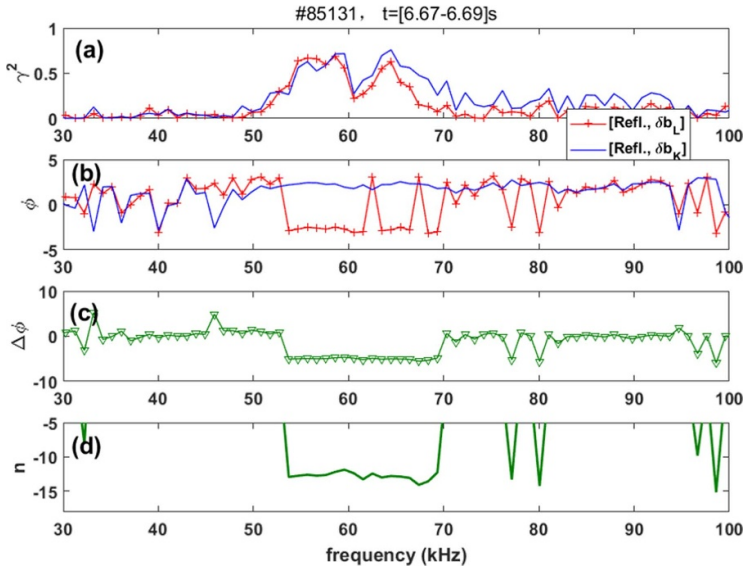

Figure 13. (*a*) and (*b*) are coherence and cross-phase between reflectometry and magnetic probe, (*c*) the phase difference of cross-phase in (*b*) and (*d*) toroidal mode number from $\Delta\phi$. It is noted that in the calculation of $\Delta\phi$ in (*c*), the cross-phase at 62.5 kHz and 67.38 kHz for [Refl, δb_L] has been corrected with a value of -2π.

Table 1. Comparison between MPM of DIII-D and EM mode of EAST.

Mode	Frequency	n	k_θ at OMP	Propagating direction in lab	Radial location	Poloidal location
MPM (DIII-D)	[40–100] kHz, multiple frequency components	3–4	0.3 cm^{-1}	EDD	Pedestal	LFS
EM mode (EAST)	[40–90] kHz, mainly two frequency components	12–13	0.41 cm^{-1}	EDD	Pedestal	Unclear

lab frame and can be observed when plasma approaching H-L back-transition. The existing time for two modes can be >100 ms. Although the frequency range for the two modes are nearly similar, the MPM has multiple frequency components (7–8) while the EM mode mainly has two frequency components (figure 3(*e*)). In addition, the MPM mode has a lower toroidal mode number (3–4) than the EM mode (12–13). Although it has been suggested that the MPM could be taken as an indicator of an impending H–L back transition but it is not yet known whether the MPM can be observed in the normal H-mode phase. The EM mode on EAST can be observed not only before the H–L back transition but also in the normal H-mode phase. It is conjectured that the MPM is an instability related to resistivity. For the EM mode studied here, an ideal MHD analysis by using ELITE code [43, 44] has been conducted. This code has been successfully applied in the pedestal stability analysis on EAST [45]. Plasma profiles at $t = 2.715$ s of discharge #87952, as shown in figure 14, have been used for the analysis. Here, the density profile was measured by reflectometry and the temperature profile was obtained from the Thomson scattering diagnostics. This case is chosen because there is a good edge T_e measurement by Thomson scattering at the EM mode persisting phase, as shown in the figure 14(*d*) where the EM mode is observed in pedestal fluctuation spectrum during the inter-ELM phase. The EM mode in this discharge, however, is weak and the correlation analysis shows very low coherence value. Therefore, the toroidal mode number cannot be analyzed. For these discharges, the coherence value is significant only if the EM mode amplitude is larger than ∼25% of the background noise level. Figure 15 shows the operational point and peeling–ballooning (P–B) stability analysis. The vertical axis is half of the peak edge current normalized by the volume averaged current density $\langle j \rangle$ and the horizontal axis is the peak values of normalized pedestal pressure gradient α. The stability boundary is defined as the growth rate of the most unstable P–B mode $\gamma = 0.5\omega_*$, where ω_* is the ion diamagnetic frequency. It is observed that the experimental operation point is far away from the stability boundary. This implies that the EM mode is not an ideal mode and resistivity could be important for the mode activity. Although the pedestal operational point is away from the ideal MHD stability boundary, the ELM still occurs later as noticed in figure 14. This phenomenon has been observed for NBI heated H-mode with high density/high pedestal collisionality ($\nu_{ped}^{*} > 3$) on EAST [46] where it shows that the resistivity effect on P–B stability is important. For the presently analyzed discharge,

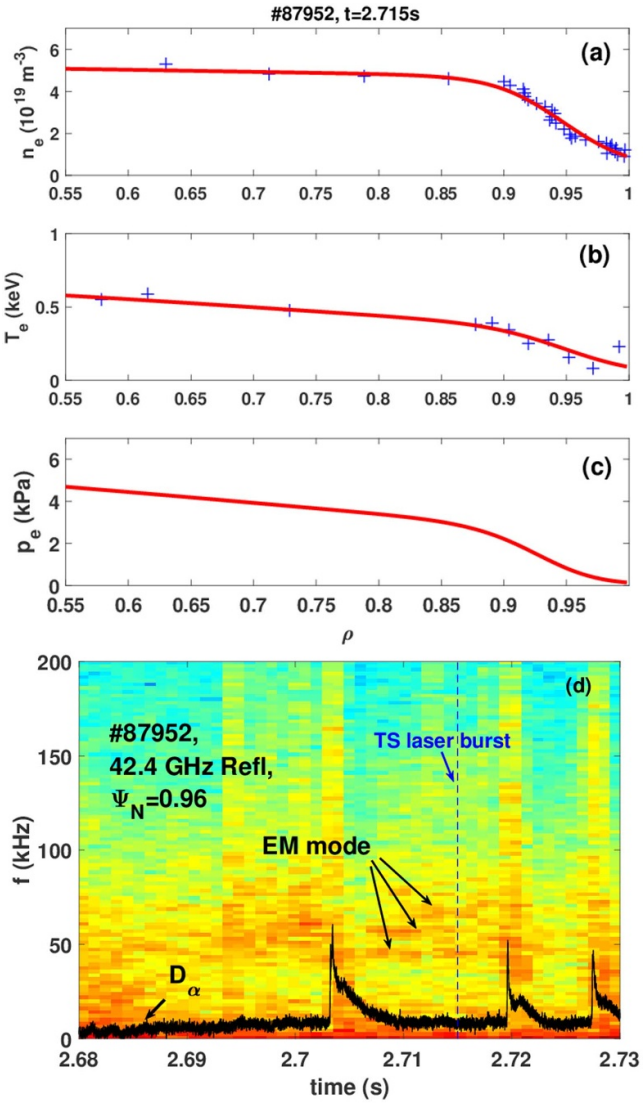

Figure 14. Plasma profiles of $t = 2.715$ s for discharge #87952 (*a*) density profile measured by DPR, (*b*) electron temperature measured by Thomson scattering, (*c*) the electron pressure profile and (*d*) shows the reflectometry fluctuation spectrum in pedestal region, where the EM mode can be observed. The vertical dashed line in (*d*) indicates the laser burst of TS diagnostics.

the pedestal collisionality is about 6 and it is expected that the resistivity effect should be considered for MHD stability calculations.

The EM mode can spread into the SOL and broaden the particle flux deposition profile in the divertor. Figures 7(*b*) and (*c*) show the time evolution of the pedestal electron density, electron temperature and electron pressure, respectively. During the long ELM-free phase before the H–L back-transition, $n_{e,ped}$ shows a gradual increase while both $T_{e,ped}$ and $p_{e,ped}$ continuously decrease. The EM mode is obviously observed in the second half phase as shown in figure 2(*e*). It seems that the density gradient destabilizes the mode. This is consistent with the result in figure 5 that the mode amplitude radial distribution coincides with the density gradient profile. The collisionality/resistivity could also be important for the mode stability as the ideal MHD analysis shows that the plasma with the mode is far away from the stability boundary shown in figure 15. Further experimental investigation and numerical simulations could help clarify the nature of the EM mode. It is found that the EM mode can spread into the SOL region as the amplitude is large enough. In TJ-II, turbulence spreading at the edge is also observed when the plasma is approaching the H–L back-transition, and this spreading is attributed to a reduction of E_r shear [15]. It is generally thought that the E_r shear is an important factor to control the turbulence spreading [14, 18], where strong E_r shear can effectively block the turbulence spreading. For our present case, there is no edge E_r measurement, but previous studies on EAST [47] shows that the E_r shearing rate decreases when the plasma approaches the H–L back-transition. A further study of how the edge E_r influences the EM mode and other pedestal turbulent mode spreading could help find an efficient method to broaden the divertor deposition profile. In the present work, only the effect of EM mode on particle flux deposition is presented. From the viewpoint of engineering, the heat flux profile is more important. However, the heat flux profile measured by the IR camera

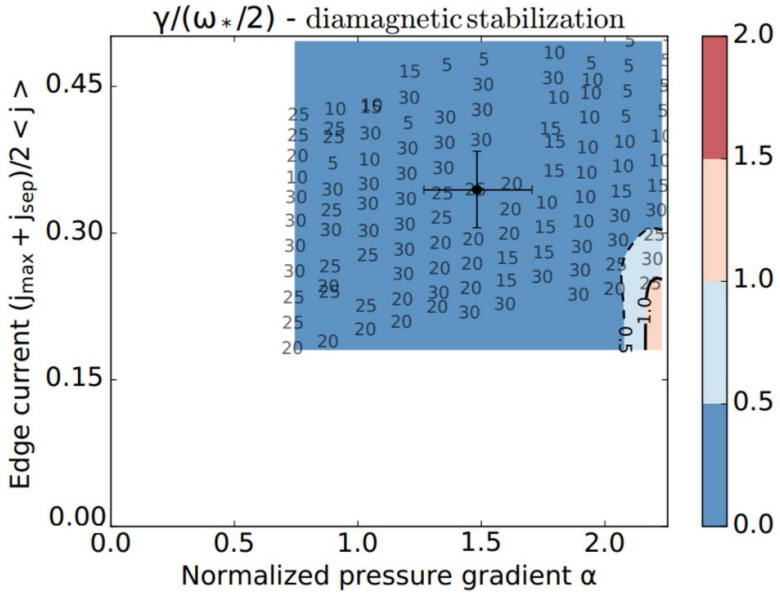

Figure 15. Idea MHD stability diagrams calculated by ELITE code with the profiles in figure 14.

for these shots is not good enough to make a conclusion and so is not shown here. This will also be left for future study.

5. Summary

In summary, an EM mode with a frequency of 40–90 kHz, toroidal mode number $n = 12$–13 and poloidal wavenumber $k_\theta = 0.41$ cm^{-1} has been observed in the pedestal gradient region of the EAST tokamak. The EM mode rotates in the EDD direction in the lab frame. It is found that the EM mode amplitude radial distribution coincides with the density gradient profile, implying that the mode is excited in the pedestal gradient region and could be destabilized by the density gradient. As the mode amplitude increases, the reflectometry channel in the far SOL with a very low density gradient can capture the EM mode, suggesting that the mode spreads from the pedestal into the SOL. In addition, the particle flux width in the divertor increases with the mode amplitude. This indicates that the mode has the effect of broadening the particle deposition profile in the divertor. The simulations in [9, 10] suggest the pedestal turbulence spreading into SOL will be an important mechanism to broaden the divertor deposition profile in future devices. Our results show that this mechanism can also play an important role even in present devices.

Acknowledgment

This work has been supported by the National Key R&D Program of China (Nos. 2022YFE03030001, 2019YFE03040002, and 2024YFE03010002) and National Natural Science Foundation of China (Nos. 11975271, 12275315 and 12305249). We thank the staff members at EAST (https://cstr.cn/31130.02.EAST), for providing technical support and assistance in data collection and analysis.

ORCID iDs

T. Zhang https://orcid.org/0000-0002-1555-6226
F.F. Long https://orcid.org/0000-0002-1008-6499
G.S. Li https://orcid.org/0000-0002-5542-1238
X.Q. Xu https://orcid.org/0000-0003-1838-9790
K.N. Geng https://orcid.org/0000-0001-7808-0192
Y.F. Wang https://orcid.org/0000-0002-0368-9566
B. Zhang https://orcid.org/0000-0003-0304-2372
K.X. Ye https://orcid.org/0000-0003-0927-4502
F.B. Zhong https://orcid.org/0000-0003-1496-9050
N. Yan https://orcid.org/0000-0002-2536-5853
X. Gao https://orcid.org/0000-0003-1885-2538

References

[1] ITER Physics Basis Editors 1999 *Nucl. Fusion* **39** 2175
[2] Wan Y. *et al* (CFETR Team) 2017 *Nucl. Fusion* **57** 102009
[3] Goldston R.J. 2012 *Nucl. Fusion* **52** 013009
[4] Eich T. *et al* (ASDEX Upgrade Team and JET EFDA Contributors) 2013 *Nucl. Fusion* **53** 093031
[5] Kukushkin A.S., Pacher H.D., Pacher G.W., Kotov V., Pitts R.A. and Reiter D. 2013 *J. Nucl. Mater.* **438** S203
[6] Eich T., Manz P., Goldston R.J., Hennequin P., David P., Faitsch M., Kurzan B., Sieglin B. and Wolfrum E. (the ASDEX Upgrade Team and the EUROfusion MST1 Team b) 2020 *Nucl. Fusion* **60** 056016
[7] Silvagni D., Eich T., Faitsch M., Happel T., Sieglin B., David P., Nille D., Gil L. and Stroth U. 2020 *Plasma Phys. Control. Fusion* **62** 045015
[8] Chang C.S. *et al* 2017 *Nucl. Fusion* **57** 116023
[9] Li Z.Y., Xu X.Q., Li N.-M., Chan V.S. and Wang X.-G. 2019 *Nucl. Fusion* **59** 046014
[10] Xu X.Q., Li N.M., Li Z.Y., Chen B., Xia T.Y., Tang T.F., Zhu B. and Chan V.S. 2019 *Nucl. Fusion* **59** 126039
[11] Garbet X., Laurent L., Samain A. and Chinardet J. 1994 *Nucl. Fusion* **34** 963
[12] Hahm T.S., Diamond P.H., Lin Z., Itoh K. and Itoh S.-I. 2004 *Plasma Phys. Control. Fusion* **46** A323

[13] Gürcan Ö.D., Diamond P.H., Hahm T.S. and Lin Z. 2005 *Phys. Plasmas* **12** 032303
[14] Wang W.X., Hahm T.S., Lee W.W., Rewoldt G., Manickam J. and Tang W.M. 2007 *Phys. Plasmas* **14** 072306
[15] Estrada T., Hidalgo C. and Happel T. 2011 *Nucl. Fusion* **51** 032001
[16] Ida K., Kobayashi T., Ono M., Evans T., McKee G. and Austin M. 2018 *Phys. Rev. Lett.* **120** 245001
[17] Jiang M. *et al* (the HL-2A Team) 2019 *Nucl. Fusion* **59** 066019
[18] Grenfell G., van Milligen B.P., Losada U., Ting W., Liu B., Silva C., Spolaore M. and Hidalgo C. (The TJ-II Team) 2019 *Nucl. Fusion* **59** 016018
[19] Choi M.J. *et al* 2021 *Nat. Commun.* **12** 375
[20] Kobayashi M., Tanaka K., Ida K., Hayashi Y., Takemura Y. and Kinoshita T. 2022 *Phys. Rev. Lett.* **128** 125001
[21] Yan Z., McKee G.R., Groebner R.J., Snyder P.B., Osborne T.H. and Burrell K.H. 2011 *Phys. Rev. Lett.* **107** 055004
[22] Diallo A., Groebner R.J., Rhodes T.L., Battaglia D.J., Smith D.R., Osborne T.H., Canik J.M., Guttenfelder W. and Snyder P.B. 2015 *Phys. Plasmas* **22** 056111
[23] Diallo A. *et al* 2014 *Phys. Rev. Lett.* **112** 115001
[24] Laggner F.M. *et al* 2016 *Plasma Phys. Control. Fusion* **58** 065005
[25] Zhong W.L. *et al* 2016 *Plasma Phys. Control. Fusion* **58** 065001
[26] Gao X., Zhang T., Han X., Zhang S.B., Kong D.F., Qu H., Wang Y.M., Wen F., Liu Z.X. and Huang C.B. (the EAST Team) 2015 *Nucl. Fusion* **55** 083015
[27] Zhang T. *et al* 2017 *Plasma Phys. Control. Fusion* **59** 065012
[28] Faitsch M., Eich T., Harrer G.F., Wolfrum E., Brida D., David P., Griener M. and Stroth U. 2021 *Nucl. Mater. Energy* **26** 100890
[29] Wu N. *et al* 2021 *Plasma Phys. Control. Fusion* **63** 075002
[30] Long F.F. *et al* (the EAST Team) 2022 *Nucl. Fusion* **62** 096018
[31] Zhou Z. *et al* 2021 *Plasma Sci. Technol.* **23** 075101
[32] Wu M.F. *et al* 2020 *J. Instrum.* **15** P12009
[33] Wang L. *et al* (the EAST Team) 2012 *Nucl. Fusion* **52** 063024
[34] Nazikian R., Kramer G.J. and Valeo E. 2001 *Phys. Plasmas* **8** 1840
[35] Diallo A., Dominski J., Barada K., Knolker M., Kramer G. and McKee G. 2018 *Phys. Rev. Lett.* **121** 235001
[36] Xu J.C. *et al* 2021 *Nucl. Fusion* **61** 096004
[37] Loarte A. *et al* 1999 *J. Nucl. Mater.* **266–269** 587
[38] Beall J.M., Kim Y.C. and Powers E.J. 1982 *J. Appl. Phys.* **53** 3933
[39] Lee J. *et al* 2014 *Rev. Sci. Instrum.* **85** 063505
[40] Wang H.Q. *et al* 2014 *Phys. Rev. Lett.* **112** 185004
[41] Chen R. *et al* 2018 *Nucl. Fusion* **58** 112004
[42] Eldon D. *et al* 2015 *Phys. Plasmas* **22** 112506
[43] Wilson H.R. *et al* 2002 *Phys. Plasmas* **9** 1277
[44] Snyder P.B. *et al* 2002 *Phys. Plasmas* **9** 2037
[45] Wang Y.F. *et al* 2018 *Plasma Phys. Control. Fusion* **60** 055002
[46] Zhong F. *et al* (the EAST Team) 2024 *Nucl. Fusion* **64** 126062
[47] Chen L. *et al* 2022 *Phys. Scr.* **97** 015601